Wearable Flexible Radio Frequency Filtering System for Muscle Contraction Monitoring

ZAYNAB ATTOUN[1] (Graduate Student Member, IEEE), NADER SHAFI[1] (Student Member, IEEE),
YOUSSEF TAWK [1] (Senior Member, IEEE), JOSEPH COSTANTINE [1] (Senior Member, IEEE),
AND ELIE SHAMMAS [2] (Senior Member, IEEE)

(Regular Paper)

[1]Electrical and Computer Engineering Department, American University of Beirut, Beirut 1007 2020, Lebanon
[2]Mechanical Engineering Department, American University of Beirut, Beirut 1007 2020, Lebanon

CORRESPONDING AUTHOR: Youssef Tawk (e-mail: yatawk@ieee.org).

ABSTRACT This paper introduces a dual band-pass and dual band-stop filter that is designed along its flexible back-end circuitry to sense and monitor muscle contractions. The filter and its back-end circuit are proposed to be wearable, flexible, and stretchable. The presented design is composed of several logarithmically scaled spiral-shaped defected ground structures (DGS) located along the ground plane of a co-planar waveguide transmission line. In addition, U-shaped slots are integrated within the transmission line to maintain the sensing operation of the filter when its structure is stretched. The entire structure is fabricated on a multi-part flexible Polyethylene Terephthalate (PET) substrate and its stretchable configuration is enabled through the integration of a Room-Temperature-Vulcanizing (RTV) silicon substrate. Such stretchable ability is obtained through the movement of the multiple parts that compose the filter and is exhibited by the tuning of its band-pass and band-stop frequencies of operation between 1 GHz and 4 GHz. Correspondingly, the stretchable ability of the filter is also indicated by the change in magnitudes of its reflection and transmission coefficients. As a result, for the band-pass operation, the insertion loss of the flexible wearable filter, placed above the human arm, at the first frequency (1.39 GHz) is -1.95 dB with a tuning range of 590 MHz, and at the second frequency (2.68 GHz) -1.94 dB with a tuning range of 330 MHz. The change in the response of the presented system is proportional to the intensity of the muscle contraction. To capture this change, a custom-designed integrated flexible back-end circuit interrogates the sensor, collects the magnitudes of the reflection and transmission coefficients, and outputs corresponding voltages. As a result, monitoring the output voltage of the back-end circuit indicates the muscle contraction level, which is sensed from the stretching movement of the filter's structure. The back-end circuit and the sensor are fabricated and tested over multiple measurement cycles where the ability of the sensor to track muscle contraction is demonstrated.

INDEX TERMS Muscle contraction monitoring, multiband filter, flexible sensor, back-end flexible circuit.

I. INTRODUCTION

The emergence of wearable technology necessitated the design of stretchable sensing circuits that are conformal to the human body. These sensors must be flexible, and able to adjust their operation to evaluate a certain mechanism or a certain biomarker. For example, flexible wearable antennas and filters have been proposed for non-invasive glucose monitoring as discussed in [1], and [2]. Electromagnetic band-gap (EBG) and soft polymer metamaterial resonators are proposed in [3]

for brain stroke diagnosis and electromagnetic head imaging. Additional wearable implementations for medical diagnostics [4], epidermal sensing for human skin monitoring [5], vital sign detection [6], heartbeat, respiration, breast cancer, and many other implementations [7], [8] leverage flexible antennas, filters, and resonators to accomplish their sensing functionalities.

Different techniques are proposed in the literature for muscle strength monitoring and evaluation. For example, in [9]

and [10] surface Electromyography (sEMG) is used to detect the contraction intensity of a muscle where the electrodes are either invasive or non-invasive. Invasive electrodes cause discomfort and pain for the users; on the other hand, non-invasive ones eliminate such discomfort while being restricted to low-frequency operation. However, in both cases, these electrodes must be connected through wires to the reading system, which limits the mobility of the users. Another approach is to use capacitive [11], [12] or resistive-based [13], [14] sensors by integrating flexible and stretchable materials. These sensors operate by monitoring the change in the capacitance or resistance when a certain pressure or strain is applied to the sensor. However, such sensors cannot be integrated with a multi-feature approach which makes them less sensitive to changes in the capacitance or resistance. Using Faraday's law of induction for muscle atrophy monitoring is investigated in [15]. The approach is based on evaluating the change in the area of a coil in a transmitter/receiver system to monitor the changes in a limb's muscle tissue size. It is also important to note that several work in the literature discusses the use of band-pass or band-stop filters for sensing applications [16], [17] where a debate exists over which type of filters offers better sensing accuracy. To that extent, in our proposed design we combine both band-stop and band-pass operation in a single sensor to maximize the accurate and sensitive estimation of the intensity of muscle contraction. More specifically, our proposed design is stretchable and composed of multiple parts that are built on a flexible PET material. All these parts are assembled together using RTV silicon that provides a bio-compatible layer, which is perfectly elastic and immune to the hysteresis effect. This layer exhibits Young's modulus of $E = 25$ MPa and Poisson's ratio $\rho = 0.48$. Such integration allows the various parts to move when stretched, causing a frequency shift in the corresponding operating frequencies.

The presented work, briefly discussed in [18], features multiple novelty aspects. First, the proposed filter exhibits dual band-pass as well as dual band-stop filtering mechanisms. This equips it with more sensing features and allows for a more rigorous data analysis, which results in better sensing accuracy as well as a higher fidelity to the changes in muscle strengths. Another novel aspect lies in the sensor's flexible design enabling its stretchable topology to conform to the shape and movement of the human arm. Hence, providing ease and comfort that is lacking from existing circuit-based sensors. Moreover, the ability to convert the frequency response into readable dc voltage levels by leveraging a customized back-end circuitry that is dedicated to this front-end sensing filter is another major novelty factor that must be taken into consideration. This back-end circuit identifies the frequencies corresponding to the magnitudes minima of the reflection and transmission coefficients of the sensor. The shift in frequencies corresponding to these minima is translated into distinctive voltages which are collected and correlated with muscle contraction levels.It is important to note that the back-end circuit and the snesor are directly integrated together
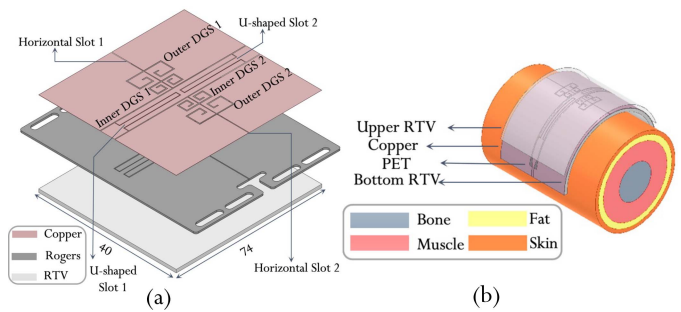

FIGURE 1. (a) The proposed topology for the stretchable filter, (b) The corresponding wearable flexible filter above a human arm.

without the need for a wired connection, which maximizes comfort and wearable ease.

The rest of the paper is divided as follows: Section II presents the design of the stretchable RF filter sensor and the transition into a wearable flexible topology. This section also includes the design of the flexible back-end circuit topology. Section III details the measurement of the various presented prototypes. Concluding remarks are drawn in the last section.

II. PROPOSED RF FILTER TOPOLOGY AND THE BACK END CIRCUITRY

In this section, we initiate our analysis by introducing a planar stretchable filter, which is then modified to serve its role as a wearable flexible sensor. The filter's response is extracted into readable values through the integration of a flexible wearable back-end circuit.

A. PLANAR STRETCHABLE RF FILTER SENSOR

A planar stretchable filter is designed at first to test the ability of the proposed structure to change its response based on an applied external force. The corresponding topology is depicted in Fig. 1(a). The first step in the design process introduces a 50 Ω Coplanar Waveguide (CPW) transmission line on a two-layer substrate with total dimensions of $74 \times 40 \times 2.31$ mm^3. The bottom substrate layer is a stretchable RTV silicon material with a thickness of 1.5 mm, a permittivity of 3.3, and a loss tangent of 0.018 [4]. The upper substrate layer is RO4003 C with a thickness of 0.81 mm, a permittivity of 3.38, and a loss tangent of 0.0021. On top of the RO4003 C, a copper conductive layer is incorporated where a 50 Ω CPW feeding line is designed with a width of $W_{CPW} = 7$ mm and separated by a gap of $G_{CPW} = 0.4$ mm from each side of the ground plane.

The second step in the design process is to incorporate the inner Spiral Defect Ground Structure (DGS) named "Inner DGS1" and "Inner DGS2" within the ground plane of the CPW transmission line as shown in Fig. 1(a). The DGS traps the energy passing from the input port to the output port resulting in a band-stop filter response. The frequency at which the energy is trapped depends on the size of the DGS [19]. The third step in the design process is based on incorporating
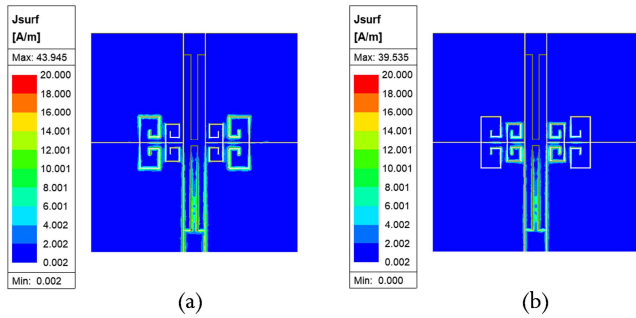
FIGURE 2. (a) Surface current distribution at 1.67 GHz and at (b) 2.27 GHz.
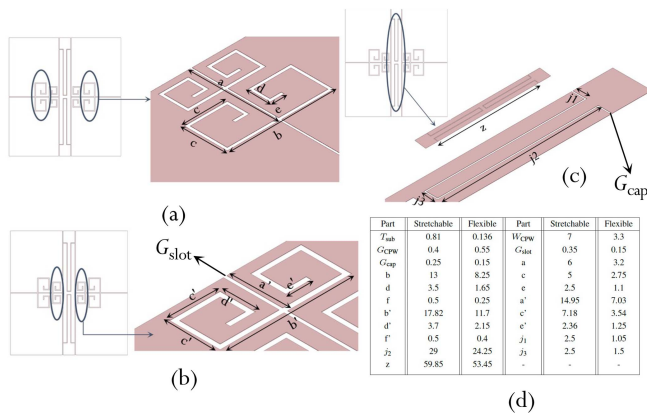

FIGURE 3. The different parts that compose (a) the two outer DGSs, (b) the two inner DGSs, (c) The U-slot along the feeding line, (d) The corresponding physical dimensions for each part.

FIGURE 4. Parametric study of the critical parameters of the filter, (a) the total lengths of the two outer and inner DGSs, (b) The widths of the gaps in the horizontal slots and the U-Slot capacitors.

two additional spiral DGSs named "Outer DGS1" and "Outer DGS2" within the ground plane of the CPW transmission as also shown in Fig. 1(a). The two outer DGSs are logarithmically scaled with respect to the inner spiral DGSs by a factor of 16, which enables a second band-stop frequency response. The band-stop operation as a result of the four DGSs is clearly highlighted by the surface current distribution displayed in Fig. 2. The fourth step of the design process focused on enabling the stretching potential of the structure. Hence, two horizontal slots with a width equal to $G_{slot} = 0.35$ mm were etched along the entire ground plane from each side of the CPW transmission line. These two slots, named "horizontal slots 1 and 2" in Fig. 1(a), are aligned along the center of the various integrated DGSs. The two horizontal slots along with the four integrated DGSs are designed to generate two band-stop frequency bands, while enabling a band-pass frequency operation between the two band-stop frequencies, in addition to facilitating the stretching mechanism. The fifth step incorporates two symmetric U-Slot capacitors of width equal to $G_{cap} = 0.25$ mm, which are etched exactly along the feeding line. These two slots, highlighted in Fig. 1(a) lead to a second band-pass frequency operation.

The various parts that compose the stretchable sensor are shown in Fig. 3, where Fig. 3(a) highlights one of the two
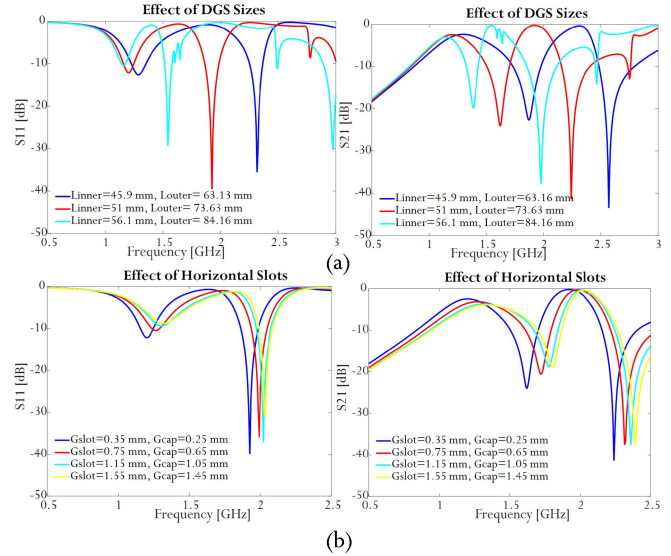
outer DGSs, Fig. 3(b) shows one of the two inner DGSs, and Fig. 3(c) displays one of the two U-shaped slots along the CPW feeding line. The corresponding physical dimensions for each part of the entire structure are summarized in Fig. 3(d). A parametric study was performed on the most critical parameters of the filter, which include: the sizes of the inner and outer spiral DGSs, the widths of the gaps in the two horizontal slots and, the widths of the gaps in the two U-Slot capacitors. At first we identified the total length of the outer DGS to be "L_{outer}" which is equal to $(a + b + (c + c + d + e) \times 2))$ in Fig. 3(a), and the total length of the inner spiral DGS to "L_{inner}" which is equal to $(a' + b' + (c' + c' + d' + e') \times 2))$ in Fig. 3(b). Shorter lengths of "L_{inner}" and "L_{outer}" result in higher frequencies of operation for the two band-stop frequencies as well as for the in-between band-pass frequency of the filter as shown in Fig. 4(a). As a result, to ensure our optimal performance at the desired frequencies of operation, we identified the best combination for "L_{inner}" and "L_{outer}" to be equal to 51 mm and 73.63 mm, respectively. For these chosen lengths, we then varied the widths of the gaps of the two horizontal slots in the ground plane "G_{slot}" and the widths of the gaps in the two U-Slot capacitors within the feeding line "G_{cap}" which influence the band-pass and band-stop operation of the filter. Wider horizontal gaps in the ground plane and the top layer of the filter result in higher resonant frequencies. These horizontal gaps greatly affect the sensitivity of the sensor to strain measurements as shown in Fig. 4(b). In our design, we opted for the $G_{slot} = 0.35$ mm, $G_{cap} = 0.25$ mm as a trade-off between sensitivity and fabrication constraints. The filter designed according to the selected dimensions, shown in Fig. 3(d) result in a dual band-stop operation at 1.67 and 2.27 GHz as well as a dual band-pass response at 1.2 and 1.95 GHz, respectively. It is important to note that for

sensing applications a narrow bandwidth is always adopted for a maximized sensitivity.

Adapting this topology to wearable apparel necessitates the re-design of this sensor on a flexible substrate. This results in a flexible wearable structure which will be discussed in the next section. Such a structure is tailored to monitor muscle contraction.

B. FLEXIBLE WEARABLE RF FILTER SENSOR

Measuring muscle contraction and evaluating muscle strength requires the integration of a flexible wearable filter as a sensor that conforms to the human body and moves along its muscle contractions. As a result, the topology of the filter presented previously is modified to be wearable and flexible while maintaining its stretchable feature.

The ability of the sensor to be flexible and conformal to the human body necessitates an appropriate selection of a suitable substrate. Multiple substrate options can be considered, however, polyethylene terephthalate (PET) and denim come to mind as the front runners. Looking into denim as a potential flexible substrate candidate necessitates resorting to sewing conductive filaments to realize the filter topology. However, sewing of the conductive filament (e-textile filament) causes a resolution problem in the various gaps of the filter topology. This is because the maximum attained resolution would be 0.5 mm according to [20], whereas the required gap width for the slots are $G_{slot} = 0.35$ mm, $G_{cap} = 0.25$ mm. Thus, the needed resolution cannot be attained to achieve the detection sensitivity for small gap variations. Furthermore, from a mechanical perspective, contrary to PET, denim is a non-uniform substrate composed of fibers, thus it has different mechanical properties in different directions. The internal fibrous structure of denim might induce non-uniform gaps which in turn complicates the sensor model and gap analysis. In other words, using denim does not map the gap dimensions to the loading value or direction [15]. Hence, we opted to rely on PET as the substrate of our design. In fact, our sensor is designed on a two-layer substrate which is the silicone RTV as a stretchable element and PET as a flexible substrate. These two substrates have close permittivity values which makes the modeling of the sensor during the design stage easier than using the silicone RTV in combination with the denim flexible substrate. This is because the permittivity values of these two materials are far from each other, where the permittivity of denim ranges from 1.4 to 1.8 and the permittivity of silicone RTV is 3.3. The corresponding topology of the flexible wearable filter is detailed in Fig. 1(b) above a model of a human arm. To achieve the required functionality, the PET substrate used in the design exhibits a thickness of 0.136 mm, a permittivity of 2.99, and a loss tangent of 5.79×10^{-3}. Moreover the integrated silicon RTV layer at the bottom of the sensor serves to collectively group the different parts that compose the filter. At the same time, a second RTV silicon layer is added to the top of the structure. This second silicon layer enhances the structure's robustness and its flexibility to varying dimensions of a human arm. Accordingly, the proposed flexible filter has

been transformed into a sensor that is conformal with muscle curvatures, and its stretching flexibility is ensured by the integration of the two RTV silicon sheets.

The design of the flexible filter to fit over a human arm necessitates evaluating the loading of the flexible filter with a four-layer human arm [21]. The various layers in the arm model represent the bone, muscle, fat, and skin as depicted in Fig. 1(b). In addition, each layer has a certain thickness with specific electrical properties in terms of dielectric constant and loss tangent [22]. The entire sensor is also separated from the human arm by an offset of 1.8 mm to ensure optimal performance. All the new dimensions of the various parts that compose the sensor are included in the table in Fig. 3(d). For example, the width of the CPW feeding line W_{CPW} is now 3.3 mm while the gap between the feeding line and the ground plane is $G_{CPW} = 0.55$ mm in order to ensure a characteristic impedance of 50 Ω at both ports when the filter is loaded with the human arm model. Furthermore, the CPW transmission line is tapered at its input and output with a tapering width $W_{tpr} = 1$ mm and a tapering gap $G_{tpr} = 0.1$ mm. These additional tapered segments are essential to enable the integration of the SCT048-SMA connectors [23] that are attached to the two ports of the sensor. All the new dimensions of the DGSs, the horizontal slots, and the U-slot capacitors are re-designed to ensure an appropriate response over a PET substrate with the integration of two RTV silicon sheets. These new dimensions preserve the operational mechanism of the filter as a dual band-stop behavior at 2.22 GHz and 3.25 GHz, as well as a dual band-pass behavior at 1.43 GHz and 2.67 GHz, respectively.

An additional parameter that was taken into account when re-designing the filter is Specific Absorption Rate (SAR), whose values must lie within the acceptable range as defined by the Federal Communications Commission (FCC) [24]. When placed above a cylindrical arm model, the proposed flexible sensor produces a SAR of: 1.457 W/Kg on the skin layer, 0.307 W/Kg on the fat layer, 0.161 W/Kg on the muscle layer, and 0.014 W/Kg on the bone level. On the other hand, when placed above a flat rectangular arm model, the proposed sensor produces a SAR of: 1.532 W/Kg on the skin layer, 0.16 W/Kg on the fat layer, 0.351 W/Kg on the muscle layer, and 0.024 W/Kg on the bone level. Hence, regardless of the geometrical model of the arm, the proposed sensor's SAR values are all within the acceptable range. All the SAR values are obtained by simulating the entire system in both arm models using Ansys High-Frequency Structure Simulator (HFSS) [25].

C. STRETCHING MECHANISM

Both proposed filters are composed of three main parts as presented in Fig. 5(a). These parts are labeled as an upper W-Part, a bottom W-Part, and an H-Part. All these parts are assembled together by attaching them to the silicon RTV layer that resides at the bottom of the sensor for the stretchable design and in the bottom and top layers for the flexible wearable structure. The assembly of the different parts of the filter
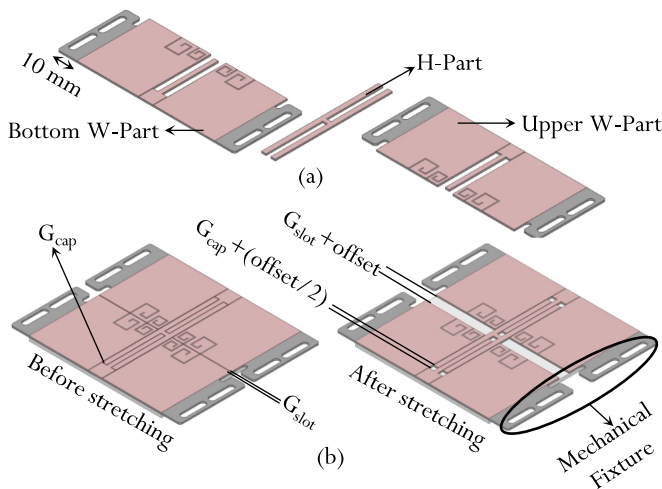
FIGURE 5. (a) The different parts of the proposed filter, (b) Stretching mechanism of the entire filter.

FIGURE 6. The different blocks that compose the back-end circuitry.

takes into account that before the stretching mechanism, the two U-shaped slots are separated from the main CPW feeding line by a specific distance G_{cap} while the two horizontal slots have a width of G_{slot} as depicted in Fig. 5(b). Accordingly, when the filter is stretched in a horizontal direction by a total displacement equal to "offset" in mm, the two W-Parts move away from each other in a horizontal movement, with an increasing amount of the gap separation, which is equal to "offset" in mm within the ground planes and "offset/2" in mm within the feeding line, as depicted in Fig. 5(b). The change in the separation between the various parts of the stretchable sensor allows a variation in the capacitance of both the inner and outer DGSs in addition to the corresponding capacitance of the two U-shaped slots. Such change entails a variation in the filter's band-stop as well as band-pass frequencies. Accordingly, the shift in the filter's reflection and transmission coefficients can be correlated to the intensity of the applied tension which in turn is related to the value of the induced displacement (i.e., "offset") between its various parts.

To accurately monitor the amount of the induced displacement in the stretchable design, a mechanical fixture is added to the structure as presented in Fig. 5(b). The purpose of this fixture is to enable the measurement of the proposed filter at different displacement positions which correspond to different stretching states. More specifically, three different values for "offset" are considered. These values correspond to 0.5 mm, 1 mm, and 1.5 mm respectively. To design the presented mechanical fixture, the rigid substrate is extended beyond the copper conductor to the right and left of the W-Parts by a distance equal to 10 mm, then four oval-shaped holes are drilled in the extended areas.

The operation mechanism of the wearable flexible sensor follows the same working principle as the stretchable design. The change in the response is obtained by varying the bending positions of the human arm which in turn entails a change in the separati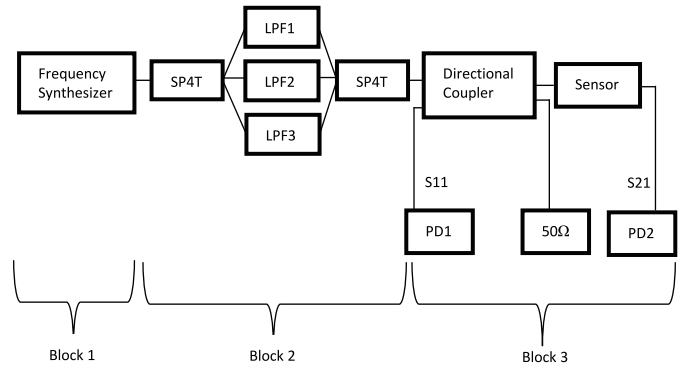on gap between the various parts that compose the flexible design. However, the integration of the RTV silicon layer on top of the structure eliminates the need for mechanical fixtures which were originally implemented in the stretchable design.

D. FLEXIBLE BACK-END CIRCUIT
A flexible back-end circuit is designed to interrogate the filter and extract its results. Hence, a flexible circuit is designed to measure the magnitude of the transmission and reflection coefficients of the sensor. This circuit analyzes and correlates the changes in the sensor's reflection coefficient (i.e., $|S_{11}|$) and transmission coefficient (i.e., $|S_{21}|$) magnitudes. More specifically, the change in the reflection coefficient response is monitored to detect the variation in the band-pass frequencies while the transmission coefficient accounts for the change in the band-stop response. Such change in the sensor's band-pass and band-stop frequencies enables quantifying the intensity of the muscular contraction. The muscle movements result in a shift in the minima of $|S_{11}|$ and $|S_{21}|$ of the sensor. Accordingly, the operating frequencies for each state of muscular contraction can be determined by allocating the location of the frequency coordinate of the minimum magnitude of $|S_{11}|$ and $|S_{21}|$. Consequently, these frequencies can be correlated to the specific intensity of muscle contraction.

The block diagram of the proposed back-end circuit is presented in Fig. 6. The circuit is composed of three main blocks: a frequency synthesizer, a harmonic suppression block, and a detection block. The frequency synthesizer provides the sensor with an excitation signal spanning from 500 MHz to 4 GHz. Since the frequency synthesizer is a nonlinear device, it generates harmonic signals in addition to the excitation signal supplied to the sensor. This can distort the output dc voltages that are read from the back-end circuit, and in return, this can distort the muscular contraction intensity value associated with it. Therefore, a harmonic suppression block is incorporated. More specifically, this block consists of two Single-Pole Four-Throw (SP4T) switches [26] and three low-pass filters (LPF) with cut-off frequencies equal to 915 MHz [27], 1920 MHz [28], and 3700 MHz [29], respectively.

This block divides the entire frequency range into three sub-ranges according to the cut-off frequencies of the low-pass filters (LPFs): the first LPF divides the frequency range from 500 MHz to 915 MHz, the second LPF divides the frequency range from 915 MHz to 1920 MHz, and the third LPF divides the frequency range from 1920 MHz to 3700 MHz. By segregating the entire frequency range into these three sub-ranges and by selecting only one of them to operate at a time using the SP4T switches, no harmonics are delivered to the sensor from the deployed frequency synthesizer.

The reflection and transmission coefficients from the filter are separated and detected by the detection block [30], [31]. This block is composed of a directional coupler [32] to separate the forward and reverse path of the signal passing through the sensor, and two power detectors [33] to enable the detection of the power level of the reflected signal (i.e., $P_{\text{out\_S11}}$) and transmitted signal (i.e., $P_{\text{out\_S21}}$). These two power levels are calculated using (1) and (2). More specifically, P_{in}, in dBm, is the input power of the excitation signal, IL_{DC}, in dB, is the insertion loss of the directional coupler, S_{11_sensor}, in dB, is the magnitude of the reflection coefficient of the filter, C_{DC}, in dB, is the coupling coefficient of the directional coupler, S_{21_sensor}, in dB, is the magnitude of the transmission coefficient of the filter.

$$P_{\text{out\_S11}} = P_{\text{in}} - IL_{\text{DC}} - S_{11\_sensor} - C_{\text{DC}} \qquad (1)$$

$$P_{\text{out\_S21}} = P_{\text{in}} - IL_{\text{DC}} - S_{21\_sensor} \qquad (2)$$

III. FABRICATION OF FILTERS AND BACK-END CIRCUIT ALONG WITH THEIR MEASUREMENT RESULTS

In this section, the fabrication and measurement of the filters are presented. The measurements of the wearable flexible system are performed on 30 different volunteers to validate its ability to monitor muscle contraction under different human arm dimensions. Finally, the implementation of the proposed back-end flexible circuit to translate the response of the flexible filter into voltage readings is detailed.

A. FILTER FABRICATION AND TESTING

Before testing the wearable filter, it is important to verify that the stretchable filter is capable of measuring various traction forces. At first, we start by detailing the fabrication and assembly process. In fact, the various parts that compose the stretchable filter are fabricated separately as depicted in Fig. 7(a). In addition, two independent mechanical holders with four holes of a diameter equal to 3.2 mm are designed to be integrated above the assembled structure in order to hold the structure at a specific displacement "offset". These two holders are also shown in Fig. 7(a). The fully assembled prototype is presented in Fig. 7(b) for two different stretching states. The various parts that compose the entire structure are combined together on an RTV silicon sheet. The entire structure is secured with Nylon M3 screws of a diameter equal to 3 mm. To change the displacement for testing the filter at another state, the screws are first undone, then the proposed
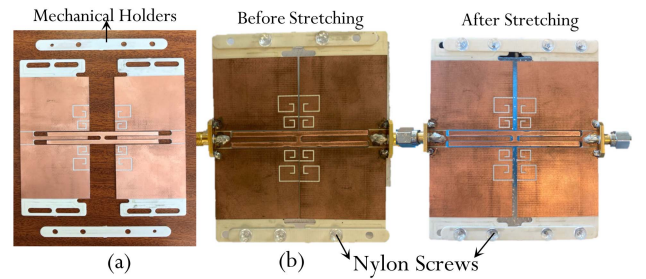

FIGURE 7. (a) The different parts that compose the stretchable filter, (b)The assembled filter with the integration of the silicon sheet in two different stretching states.

TABLE 1 Band-Pass Frequencies of the Planar Stretchable RF Filter at Different States

Frequency	State 0	State 1	State 2	State 3
First Band	1.2	1.23	1.3	1.32
Second Band	1.95	2.02	2.07	2.09

filter is stretched to the required new displacement, and finally, it is secured again by re-tightening the screws.

When a certain level of tensile force is applied to the stretchable sensor, the various parts that compose its structure move away from each other in line with the applied strain. This leads to an increasing displacement between the two W-parts as well as between the H-part and the main feeding line. Therefore, to test the filter's ability in strain and tension sensing, the overall structure is stretched to various displacements. First, the sensor is tested at its initial state (state 0) with initial gaps equal to $G_{slot} = 0.35$ mm in the ground planes and $G_{cap} = 0.25$ mm in the feeding line. Then, the filter is stretched to multiple displacements identified as "offset" in mm. After stretching, the initial gaps in the ground planes increase by "offset" and the initial gaps in the feeding line increase by "offset/2". For state 1, "offset" is 0.5 mm, then 1 mm for state 2 and finally 1.5 mm for state 3. A comparison between the simulated and measured $|S_{11}|$ (i.e., reflection coefficient in dB) and $|S_{21}|$ (i.e., transmission coefficient in dB) of the proposed stretchable filter at different stretching states are shown in Fig. 8. An agreement is obtained between both the simulated and measured data, thus validating the proposed approach in reconfiguring the filter's response due to the induced displacement that maps to a certain level of applied tension.

It is clear from the obtained results that when the displacement increases, the band-pass and band-stop frequencies of the filter shift gradually with respect to the stretching degree. Table 1 presents the two measured band-pass frequencies at each stretching state. The first frequency band increases from 1.2 GHz (State 0) to 1.23 GHz for 0.5 mm displacement (State 1), then from 1.23 GHz to 1.3 GHz for 1 mm displacement (State 2), and finally from 1.3 GHz to 1.32 GHz for 1.5 mm displacement (State 3). The second band-pass frequency band
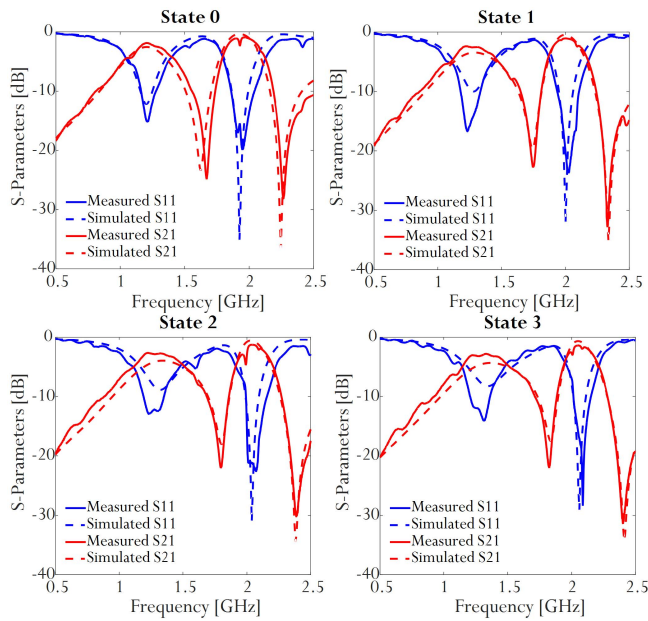
FIGURE 8. Comparison of the simulated and measured S-parameters results at different stretching states of the stretchable filter prototype.

TABLE 2 Band-Stop Frequencies of the Planar Stretchable RF Filter at Different States

Frequency	State 0	State 1	State 2	State 3
First Band	1.67	1.75	1.8	1.83
Second Band	2.27	2.33	2.39	2.4

increases from 1.95 GHz (State 0) to 2.02 GHz for 0.5 mm displacement (State 1), then from 2.02 GHz to 2.07 GHz for 1 mm displacement (State 2), and finally from 2.07 GHz to 2.09 GHz for 1.5 mm displacement (State 3). Table 2 shows the two measured band-stop operating frequencies at each stretching state. The first band-stop operating frequency band increases from 1.67 GHz (State 0) to 1.75 GHz for 0.5 mm displacement (State 1), then from 1.75 GHz to 1.8 GHz for 1 mm displacement (State 2), and from 1.8 GHz to 1.83 GHz for 1.5 mm displacement (State 3). On the other hand, the second band-stop frequency band increases from 2.27 GHz (State 0) to 2.33 GHz for 0.5 mm displacement (State 1), from 2.33 GHz to 2.39 GHz for 1 mm displacement (State 2), and from 2.39 GHz to 2.4 GHz for 1.5 mm displacement (State 3). These results validate the ability of the proposed prototype to behave as a sensor that indicates any applied level of strain by monitoring the shift in $|S_{11}|$ and $|S_{21}|$ over the four operating bands, which are displayed within the reflection and transmission coefficients. Since the ability of this embodiment of the sensor is proven, now we can verify the ability of the wearable and flexible filter to indicate muscle contraction levels.

Fabricating the flexible and wearable filter must debut with the fabrication of its different parts. These parts, shown in
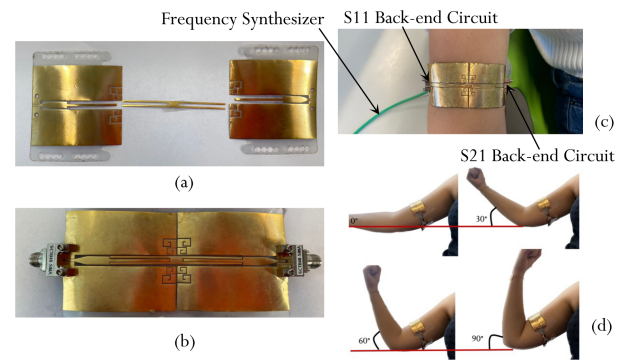

FIGURE 9. (a) The different parts that compose the flexible filter, (b) The assembled flexible filter prototype, (c) The flexible filter on top of a human arm, (d) The different states of the filter over the arm of a volunteer during the testing phase.

Fig. 9(a), are then assembled together to form the final prototype displayed in Fig. 9(b) with a total dimension of 40 × 92 × 3.371 mm^3. To enable its conformal operation, two silicon RTV sheets are integrated on the top and bottom layers of the flexible PET-based substrate. The corresponding fabricated prototype placed above a human arm is presented in Fig. 9(c). To confirm the ability of the proposed wearable flexible filter sensor to accurately sense and monitor muscle contractions, the fabricated prototype is tested according to the measurement setup summarized in Fig. 9(d). More specifically, the setup is based on placing the flexible filter sensor on the bicep of a volunteer, then the volunteer is asked to bend the arm over four different angles, state 1: 0°, state 2: 30°, state 3: 60°, and state 4: 90° with respect to the floor. When the angle of the arm with the horizontal axis increases, the bending radius of the bicep increases due to a change in the flexing angle, which forces the two W-parts of the sensor to move away from each other accordingly. This leads to an increase in the horizontal G_{slot} and U-slots gaps G_{cap}, which produces a shift in $|S_{11}|$ and $|S_{21}|$ responses of the filter proportionally with the intensity of the movement and hence the muscular contraction. Thus, by monitoring the change in the operating frequencies of the filter, the intensity of the muscular contraction is evaluated.

Thirty volunteers of different ages, genders, fat distribution, muscle content, and arm circumference participated in this study. The volunteers were divided equally between males and females and they all signed a consent form before participating in this study. The measured shift in the band-pass (i.e., $|S_{11}|$) frequencies with respect to the flexing angle of six different volunteers, are shown in Fig. 10(a) for the first band-pass frequency and in Fig. 10(b) for the second band-pass frequency. Also, Fig. 10(c) shows the filter's response from these volunteers for the first band-stop frequency while Fig. 10(d) highlights the measured results for the second band-stop frequency. It is clear from the presented data in these four figures that when the flexing angle increases due to muscle contraction, the corresponding frequencies shift
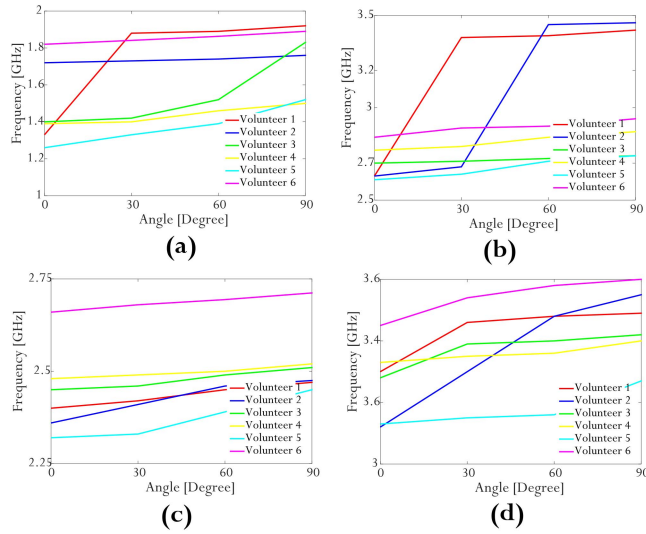
FIGURE 10. The corresponding shift in the $|S_{11}|$ and $|S_{21}|$ frequencies of the flexible filter for different flexing angles of the first six volunteers: (a) The first band-pass frequency, (b) The second band-pass frequency, (c) The first band-stop frequency, (d) The second band-stop frequency.

proportionally with the intensity of the contraction of the muscle. It is important to note that this filter is designed with the human body taken into consideration from the simulation stage. Hence, it is optimized to operate over a human arm, whose dielectric properties may vary from user to user based on different parameters. On the other hand, the main feature this sensor monitors is the change in the magnitude of the S-parameters for the different bending angles for each volunteer. It may happen in rare cases that two volunteers exhibit similar magnitudes for the same bending angles, a feature that can be attributed to their respective body compositions. However, the main focus is always to monitor the change of the magnitudes between different angles regardless of the body type. In addition, it is important to note that throughout the entire study and measurement results, the trend of variation of the corresponding frequencies is the same with respect to the change in the bending angle as highlighted in Fig. 10.

Furthermore, the sensor is resilient to mechanical deformations because the used copper pads have a much higher Young's modulus [34] than the stretchable silicone substrate which is elastic. Thus, the stretching and deflection will only affect the horizontal gaps which are made of the perfectly elastic silicone RTV. Once the sensor is finalized, repeatable gaps and displacements are obtained because the silicone is perfectly elastic. Any non-linearity in the frequency response of the sensor due to gap dimensions can be captured and compensated in the initial realization process.

B. FLEXIBLE BACK-END CIRCUIT

The proposed back-end circuit is fabricated in two parts. The first part, shown in Fig. 11(a), includes the harmonic suppression and detection blocks to detect the power level of P_{out_S11}, and the second part, shown in Fig. 11(b), includes only a power detector to detect the power level of P_{out_S21}.
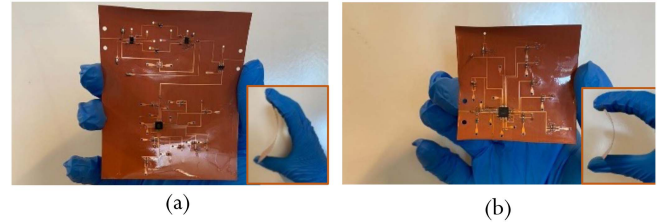

FIGURE 11. The fabricated back-end circuit on a flexible PET substrate to detect (a) $|S_{11}|$ and (b) $|S_{21}|$.

TABLE 3 Voltage Measurements of the Reflection Coefficient of the Sensor Using the Back-End Circuit at Different States

1st Band	Freq.	State 0	State 1	State 2	State 3
	1.5	**0.284**	0.288	0.303	0.328
	2.3	0.286	**0.285**	0.312	0.334
	2.4	0.298	0.287	0.296	0.337
	2.5	0.293	0.293	**0.291**	0.331
	2.6	0.32	0.294	0.295	**0.328**
2nd Band	3	0.295	0.335	0.335	0.343
	3.1	**0.288**	0.31	0.31	0.308
	3.2	0.33	**0.301**	0.323	0.284
	3.3	0.305	0.314	**0.321**	0.286
	3.4	0.297	0.321	0.325	**0.28**
	3.5	0.281	0.307	0.307	0.315

The bold values are the voltage levels.

TABLE 4 Voltage Measurements of the Transmission Coefficient of the Sensor Using the Back-End Circuit at Different States

1st Band	Freq.	State 0	State 1	State 2	State 3
	2.5	**0.4**	0.403	0.49	0.361
	2.65	0.539	**0.337**	0.49	0.859
	2.75	0.562	0.398	**0.381**	0.357
	2.8	0.534	0.433	0.577	**0.359**
2nd Band	3.55	**0.421**	0.367	0.515	0.396
	3.65	0.425	**0.318**	0.573	0.395
	3.7	0.545	0.321	**0.347**	0.392
	3.75	0.543	0.319	0.35	**0.339**

The bold values are the voltage levels.

To validate the performance of the entire system in detecting the frequency shift in the $|S_{11}|$ and $|S_{21}|$, the two parts of the back-end circuit are connected together to the two ports of the flexible filter and placed on a volunteer's arm as shown in Fig. 9(c). The power detectors are biased appropriately by connecting them to a 5 V power supply [33]. The activation of the switches is done by connecting them to the same biasing voltage to select the required LPF path for measurements. The frequency of the excitation signal generated from the frequency synthesizer is swept with a constant input power P$_{in}$ of 10 dBm. For each discrete frequency, the output dc voltages of the back-end circuit are recorded where the voltage

TABLE 5 Table of Comparison Between Our Proposed Wearable Sensor and Other Wearable Sensors Present in the Literature

Paper	Type of Material	Flexible/Stretchable	Frequency [GHz]	Wearable	Tunablity [MHz]/Band	Device Type
[35]	PDMS	Stretchable	5.674	No	141	Antenna
[36]	PDMS	Stretchable	2.37	No	100	Antenna
[37]	silicon	Stretchable	9.61/10.28	No	0.03/0.01	Antenna
[38]	Teflon	Flexible	2.4	Yes	248	PIFA
[39]	Teflon	Flexible	2.4	Yes	400	PIFA and PLL
[40]	Textile	Stretchable	2.4	Yes	440	Antenna
[41]	PDMS	Stretchable	0.76	Yes	150	Antenna
Our Work	Silicon RTV	Stretchable and Flexible	1.43/2.22/2.67/3.25	Yes	210/530/330/490	Full System

TABLE 6 Table of Comparison Between Our Proposed Flexible Wearable Filter Sensor and Other Filter Sensors Present in the Literature

Paper	Frequency [GHz]	Insertion Loss [dB]	Frequency Bands	Material	Wearable
[42]	2.45	-1.5	Single band	RT/Duroid5880	Yes
[43]	2	-1.3	Wideband	PDMS	Yes
[44]	1.9	-2.8	Single band	Rogers RO6010	No
[45]	1.5	-2.5	Wideband	Rogers RO4003C	No
[46]	1.75	-5	Single band	Rogers RO4003	No
Our Work	1-4	-1.95	Multiband	PET and RTV	Yes

values are proportional to $|S_{11}|$ and $|S_{21}|$. The recorded dc voltage values of the performed measurements for one of the thirty volunteers using the back-end circuit are summarized in Tables 3 and 4.

Table 3 shows that the minimum dc voltage for the first $|S_{11}|$ band resides at 1.5 GHz when the filter is at its initial state (state 0). When the filter is stretched to state 1, the minimum dc voltage value shifts to 2.3 GHz, then to 2.5 GHz at state 3, and finally to 2.6 GHz for state 4. As for the second $|S_{11}|$ band, the minimum dc voltage resides at 3.1 GHz when the filter is at state 0, shifts to 3.2 GHz at state 1, then 3.3 GHz at state 3, and finally at state 4 the minimum dc voltage shifts to 3.4 GHz. Similarly, Table 4 shows that the minimum dc voltage for the first $|S_{21}|$ band resides at 2.5 GHz when the filter is at state 0 and shifts to 2.8 GHz for state 4. As for the second $|S_{21}|$ band, the first minimum dc voltage resides at 3.55 GHz and moves progressively to 3.65 GHz, then 3.7 GHz until it reaches 3.75 GHz for the final state.

Consequently, when the filter is stretched due to arm contractions, the minima of $|S_{11}|$ and $|S_{21}|$ where the minimum dc voltage resides are shifted based on the intensity of muscular contractions. Thus, by detecting the frequency where the minimum voltage resides, the operating frequency can be detected, which provides information about the intensity of the muscular contraction. It is worth mentioning that the term "minimum" here corresponds to the point where the slope of $|S_{11}|$ and $|S_{21}|$ changes from decreasing to increasing, and the code only takes into account the first two minima that occur within a cycle, e.g. one sweep cycle of the exciting signal from 1 GHz to 4 GHz.

The proposed filter was designed and fabricated with the user's comfort in mind. It is realized using flexible, stretchable, and lightweight material which provides conformity when the filter is placed and bent on the arm of different users. The back-end circuit is also designed using the same lightweight flexible material. In addition, this back-end circuit is directly connected to the sensor without the need for wires connecting the sensor to a receiving end which can create discomfort and be constraining for the user.

Table 5 shows a comparison between our work presented herein and other work found in the literature. The existing wearable and stretchable RF sensors operate by monitoring the frequency shift over a single frequency band whereas our work monitors the shift in the minimum of $|S_{11}|$ and $|S_{21}|$ across four operational frequencies. Such a mechanism displays a higher sensitivity with more data points for analysis when monitoring the muscle contraction. In addition, the presented work in this paper proposes a full system with the corresponding flexible back-end circuitry that translates the shift in the band-pass and band-stop frequencies into readable dc voltage levels. In addition, Table 6 compares other band-pass filter sensors present in the literature with our proposed filter sensor in terms of frequency, the number of bands, the insertion loss, and whether it is wearable or not. It is noted from Table 6 that most work in the literature focuses on either a band-pass or band-stop operation, while our proposed sensor integrates both. Furthermore, most of the work in the literature presents either a single band or wideband operation while our presented design features multi-band operation. The function of our proposed filter as a wearable sensor thrives

on the multi-band band-pass/band-stop operation to output accurate muscle contraction evaluations with high sensitivity.

IV. CONCLUSION

A stretchable RF filter that is adapted to be flexible and wearable above a human arm for muscle contraction monitoring is presented in this paper. The proposed filter is implemented with a CPW topology complemented by etched DGSs and capacitors from the ground planes and feeding line respectively. Measurements demonstrated the ability of the filter to sense the intensity of the applied external force for the stretchable filter and also the muscular contractions for the flexible topology. In addition, a flexible back-end circuit that detects the shift in the minimum magnitudes of the reflection and transmission coefficients is designed, fabricated, and measured. When placed over a contracting muscle, the proposed system exhibits a change in its frequency response, which is then translated into a voltage that is communicated and analyzed. The flexible wearable system is tested on 30 volunteers with different muscular strengths. It is important to note that the proposed flexible wearable sensing system find applications in many other implementations that vary from athlete's muscle fatigue prevention, muscle health monitoring for the elderly, and rehabilitation after an injury, to assisting patients with cognitive disorders, as well as monitoring the muscle health of astronauts in long-lasting space missions.

REFERENCES

[1] J. Hanna et al., "Noninvasive, wearable, and tunable electromagnetic multisensing system for continuous glucose monitoring, mimicking vasculature anatomy," *Sci. Adv.*, vol. 6, no. 24, 2020, Art. no. eaba5320. [Online]. Available: https://www.science.org/doi/abs/10.1126/sciadv.aba5320

[2] M. Bteich et al., "A non-invasive flexible glucose monitoring sensor using a broadband reject filter," *IEEE J. Electromagn., RF, Microw. Med. Biol.*, vol. 5, no. 2, pp. 139–147, Jun. 2021.

[3] A. S. M. Alqadami, K. S. Bialkowski, A. T. Mobashsher, and A. M. Abbosh, "Wearable electromagnetic head imaging system using flexible wideband antenna array based on polymer technology for brain stroke diagnosis," *IEEE Trans. Biomed. Circuits Syst.*, vol. 13, no. 1, pp. 124–134, Feb. 2019.

[4] A. S. M. Alqadami, N. Nguyen-Trong, A. E. Stancombe, K. Bialkowski, and A. Abbosh, "Compact flexible wideband antenna for on-body electromagnetic medical diagnostic systems," *IEEE Trans. Antennas Propag.*, vol. 68, no. 12, pp. 8180–8185, Dec. 2020.

[5] C. Occhiuzzi, S. Parrella, F. Camera, S. Nappi, and G. Marrocco, "Rfid-based dual-chip epidermal sensing platform for human skin monitoring," *IEEE Sensors J.*, vol. 21, no. 4, pp. 5359–5367, Feb. 2021.

[6] C.-H. Tseng, L.-T. Yu, J.-K. Huang, and C.-L. Chang, "A wearable self-injection-locked sensor with active integrated antenna and differentiator-based envelope detector for vital-sign detection from chest wall and wrist," *IEEE Trans. Microw. Theory Techn.*, vol. 66, no. 5, pp. 2511–2521, May 2018.

[7] S.-G. Kim, G.-H. Yun, and J.-G. Yook, "Compact vital signal sensor using oscillation frequency deviation," *IEEE Trans. Microw. Theory Techn.*, vol. 60, no. 2, pp. 393–400, Feb. 2012.

[8] I. M. Danjuma, M. O. Akinsolu, C. H. See, R. A. Abd-Alhameed, and B. Liu, "Design and optimization of a slotted monopole antenna for ultra-wide band body centric imaging applications," *IEEE J. Electromagn., RF, Microw. Med. Biol.*, vol. 4, no. 2, pp. 140–147, Jun. 2020.

[9] P. Pakosz and M. Konieczny, "Training induced fatigability assessed by sEMG in pre-olympic ice-skaters," *Sci. Rep.*, vol. 10, 2020, Art. no. 14199.

[10] M. Ergeneci, D. Carter, and P. Kosmas, "sEMG onset detection via bidirectional recurrent neural networks with applications to sports science," *IEEE Sensors J.*, vol. 22, no. 19, pp. 18751–18761, Oct. 2022.

[11] H. Xue, F. Li, H. Zhao, X. Lin, and T. Zhang, "A paper-based iontronic capacitive pressure sensor for human muscle motion monitoring," *IEEE Electron Device Lett.*, vol. 43, no. 12, pp. 2165–2168, Dec. 2022.

[12] J. Tao et al., "Real-time pressure mapping smart insole system based on a controllable vertical pore dielectric layer," *Microsyst. Nanoeng.*, vol. 6, 2020, Art. no. 62.

[13] J. T. Alvarez et al., "Towards soft wearable strain sensors for muscle activity monitoring," *IEEE Trans. Neural Syst. Rehabil. Eng.*, vol. 30, pp. 2198–2206, 2022.

[14] S. Baloda, Z. A. Ansari, S. Singh, and N. Gupta, "Development and analysis of graphene nanoplatelets (GNPs)-based flexible strain sensor for health monitoring applications," *IEEE Sensors J.*, vol. 20, no. 22, pp. 13302–13309, Nov. 2020.

[15] A. Rice and A. Kiourti, "A stretchable, conductive thread-based sensor towards wearable monitoring of muscle atrophy," *IEEE Trans. Biomed. Eng.*, vol. 70, no. 8, pp. 2454–2462, Aug. 2023.

[16] R. Baghbani, M. Rad, and A. Ali, "Microwave sensor for non-invasive glucose measurements design and implementation of a novel linear," *IET Wireless Sensor Syst.*, vol. 5, pp. 51–57, 2015.

[17] H. Choi et al., "Design and in vitro interference test of microwave noninvasive blood glucose monitoring sensor," *IEEE Trans. Microw. Theory Techn.*, vol. 63, no. 10, pp. 3016–3025, Oct. 2015.

[18] Z. Attoun, N. Shafi, Y. Tawk, J. Costantine, and E. Shammas, "Wearable flexible body-adaptable frequency reconfigurable filter for muscle contraction monitoring," in *Proc. IEEE Int. Symp. Antennas Propag. USNC-URSI Radio Sci. Meeting*, 2023, pp. 781–782.

[19] W. Su, B. S. Cook, and M. M. Tentzeris, "Additively manufactured microfluidics-based "peel-and-replace" RF sensors for wearable applications," *IEEE Trans. Microw. Theory Techn.*, vol. 64, no. 6, pp. 1928–1936, Jun. 2016.

[20] L. Zhang, Z. Wang, and J. L. Volakis, "Textile antennas and sensors for body-worn applications," *IEEE Antennas Wireless Propag. Lett.*, vol. 11, pp. 1690–1693, 2012.

[21] M. Li et al., "Comparable investigation of characteristics for implant intra-body communication based on galvanic and capacitive coupling," *IEEE Trans. Biomed. Circuits Syst.*, vol. 13, no. 6, pp. 1747–1758, Dec. 2019.

[22] Jul. 2023. [Online]. Available: https://itis.swiss/virtual-population/tissue-properties/database/dielectric-properties/

[23] SMA, "Female (Jack) PCB connector edge mount. 007 inch pin, solder," *Fairview Microwave*. [Online]. Available: https://www.fairviewmicrowave.com/sma-female-standard-edge-mount-0.007-pin-pcb-connector-sct048-sma-p.aspx

[24] FCC, "Specific absorption rate (SAR) for cellular telephones," 2019. [Online]. Available: https://www.fcc.gov/general/specific-absorption-rate-sar-cellular-telephones

[25] HFSS, ANSYS, Canonsburg, PA, USA, 2022. [Online]. Available: https://www.ansys.com/products/electronics/ansys-hfss

[26] "SKY13322-375LF SP4T switch," Skyworks. [Online]. Available: https://www.skyworksinc.com/Products/Switches/SKY13322-375LF

[27] *902 MHz LPF, Kyocera AVX*. [Online]. Available: https://datasheets.kyocera-avx.com/lp0805.pdf

[28] *1880 MHz LPF, Kyocera AVX*. [Online]. Available: https://datasheets.kyocera-avx.com/lp0805.pdf

[29] *3.5 GHz Johanson LPF Technology*. [Online]. Available: https://www.johansontechnology.com/low-pass-filters

[30] V. Solomko et al., "RF impedance sensor for antenna-tuning front ends," *IEEE Trans. Microw. Theory Techn.*, vol. 68, no. 3, pp. 1095–1102, Mar. 2020.

[31] A. Salim, A. H. Naqvi, A. D. Pham, and S. Lim, "Complementary split-ring resonator (CSRR)-loaded sensor array to detect multiple cracks: Shapes, sizes, and positions on metallic surface," *IEEE Access*, vol. 8, pp. 151804–151816, 2020.

[32] D17 W Directional Coupler, "Mini-circuits." [Online]. Available: https://www.minicircuits.com/pdfs/D17W+.pdf

[33] HMC1021 Power Detector, "Analog devices." [Online]. Available: https://www.analog.com/media/en/technical-documentation/data-sheets/hmc1021.pdf

[34] L. Xu, X. Xie, and H. Fan, "Polycrystalline aggregates in the thin-wire configuration," *J. Appl. Phys.*, vol. 110, 2011, Art. no. 084909.

[35] J.-H. Low, P.-S. Chee, and E.-H. Lim, "Deformable liquid metal patch antenna for air pressure detection," *IEEE Sensors J.*, vol. 20, no. 8, pp. 3963–3970, Apr. 2020.

[36] T. Rai, P. Dantes, B. Bahreyni, and W. S. Kim, "A stretchable RF antenna with silver nanowires," *IEEE Electron Device Lett.*, vol. 34, no. 4, pp. 544–546, Apr. 2013.

[37] A. Ibrahim and D. Cumming, "Passive single chip wireless microwave pressure sensor," *Sensors Actuators A, Phys.*, vol. 165, no. 2, pp. 200–206, 2011. [Online]. Available: https://www.sciencedirect.com/science/article/pii/S0924424710004784

[38] Y.-J. An, B.-H. Kim, G.-H. Yun, S.-W. Kim, S.-B. Hong, and J.-G. Yook, "Flexible non-constrained RF wrist pulse detection sensor based on array resonators," *IEEE Trans. Biomed. Circuits Syst.*, vol. 10, no. 2, pp. 300–308, Apr. 2016.

[39] S. W. Kim, S. B. Choi, Y.-J. An, B.-H. Kim, D. W. Kim, and J.-G. Yook, "Heart rate detection during sleep using a flexible RF resonator and injection-locked PLL sensor," *IEEE Trans. Biomed. Eng.*, vol. 62, no. 11, pp. 2568–2575, Nov. 2015.

[40] M. el Gharbi, R. Fernández-García, and I. Gil, "Embroidered wearable antenna-based sensor for real-time breath monitoring," *Measurement*, vol. 195, 2022, Art. no. 111080.

[41] Y. Huang et al., "Self-similar design for stretchable wireless LC strain sensors," *Sensors Actuators A, Phys.*, vol. 224, pp. 36–42, 2015. [Online]. Available: https://www.sciencedirect.com/science/article/pii/S0924424715000060

[42] F. Benassi, G. Paolini, D. Masotti, and A. Costanzo, "A wearable flexible energy-autonomous filtenna for ethanol detection at 2.45 Ghz," *IEEE Trans. Microw. Theory Techn.*, vol. 69, no. 9, pp. 4093–4106, Sep. 2021.

[43] W. Chen, Y. Li, R. Li, A.-Y. Thean, and Y.-X. Guo, "Bendable and stretchable microfluidic liquid metal-based filter," *IEEE Microw. Wireless Compon. Lett.*, vol. 28, no. 3, pp. 203–205, Mar. 2018.

[44] Z. Shaterian and M. Mrozowski, "Multifunctional bandpass filter/displacement sensor component," *IEEE Access*, vol. 11, pp. 27012–27019, 2023.

[45] C.-H. Chio, K.-W. Tam, and R. Gómez-García, "Filtering angular displacement sensor based on transversal section with parallel-coupled-line path and U-shaped coupled slotline," *IEEE Sensors J.*, vol. 22, no. 2, pp. 1218–1226, Jan. 2022.

[46] M. Amirian, G. Karimi, B. D. Wiltshire, and M. H. Zarifi, "Differential narrow bandpass microstrip filter design for material and liquid purity interrogation," *IEEE Sensors J.*, vol. 19, no. 22, pp. 10545–10553, Nov. 2019.